ESTIMATION OF MICROSEISMIC SOURCE PARAMETERS BY 2D ANISOTROPIC WAVEFORM INVERSION

OSCAR JARILLO MICHEL and ILYA TSVANKIN

Center for Wave Phenomena, Colorado School of Mines, Golden, CO 80401, U.S.A.
ojarillo@mymail.mines.edu; ilya@dix.mines.edu

(Received June 30, 2015; accepted August 1, 2015)

ABSTRACT

Jarillo Michel, O. and Tsvankin, I., 2015. Estimation of microseismic source parameters by 2D anisotropic waveform inversion. *Journal of Seismic Exploration*, 24: 379-400.

Waveform inversion (WI), which has been used primarily for high-resolution velocity analysis, can also be employed to obtain the source parameters of microseismic events. Here, we implement WI to estimate the location, origin time, and seismic moment tensor of microseismic sources embedded in VTI (transversely isotropic with a vertical symmetry axis) media. The algorithm operates with 2D multicomponent wavefields modeled using an elastic anisotropic finite-difference code. The gradient of the objective function for the three classes of parameters is calculated with the adjoint-state method. Although in the current algorithm the VTI parameters are assumed to be known, they can be included in WI at almost no additional cost. Synthetic tests for data from layered VTI media recorded by vertical receiver arrays show that it is possible to tightly constrain all source parameters, if a sufficiently accurate initial model is available. In particular, the source location can be estimated simultaneously with the moment tensor. The resolution of event location, however, somewhat decreases when the origin time is unknown or there is an error in one of the VTI parameters.

KEY WORDS: waveform inversion, microseismic, anisotropy, transverse isotropy, multicomponent data, elastic wavefield.

INTRODUCTION

Waveform inversion is a nonlinear optimization technique, which is designed to include the entire seismic trace in building subsurface models. As first suggested by Lailly (1983) and Tarantola (1984), back-propagation in time

0963-0651/15/$5.00

of the data residuals followed by cross-correlation of the resulting wavefield with the forward-propagated wavefield helps iteratively produce high-resolution velocity models. An overview of the progress in applying WI to exploration-related problems can be found in Virieux and Operto (2009). Although WI has been mostly used in velocity analysis, information contained in seismic waveforms can constrain other important quantities, such as parameters of earthquake sources.

Recently, waveform inversion has been extended to elastic and anisotropic media (Lee et al., 2010; Kamath and Tsvankin, 2013), which makes it appropriate for multicomponent reflection and microseismic data. Also, WI has been employed to estimate earthquake source parameters in global seismology (Tromp et al., 2005; Liu and Tromp, 2006; Kim et al., 2011) and geothermal studies (Morency and Mellors, 2012). These techniques incorporate the adjoint-state method (Lions, 1972; Plessix, 2006; Fichtner, 2006, 2009) as a practical way to calculate the gradient of the WI objective function (Talagrand and Courtier, 1987) using only two numerical-modeling simulations.

Microseismic monitoring of hydraulic fractures has become an important technology in the development of unconventional shale reservoirs (Maxwell, 2010; Kendall et al., 2011). Whereas the main goal of microseismic surveys is to estimate the source locations $\mathbf{x}^s$, it is also essential to obtain the event origin time t_0 and the source moment tensor $\mathbf{M}$. In practice, the inversion for $\mathbf{M}$ is typically performed separately under the assumption that the source has been located. In contrast, WI has the potential of resolving all these parameters simultaneously and with higher accuracy from multicomponent seismic data.

Reliable microseismic event location depends on the accuracy of the employed velocity model. Because hydraulic fracturing is typically applied in anisotropic shale formations, building realistic velocity models that account for seismic anisotropy is particularly important. For example, Grechka et al. (2011) and Li et al. (2013) demonstrate that anisotropic velocity fields constructed from traveltimes while locating microseismic events provide more accurate source locations than those obtained using conventional isotropic techniques. As shown by Grechka and Yaskevich (2013, 2014), for microseismic surveys with sufficient angle coverage it is possible to construct even layered triclinic (i.e., most general anisotropic) models and substantially improve the accuracy of event location.

However, because existing kinematic techniques invert traveltimes of direct arrivals, the resolution of event location is subject to the Rayleigh criterion (i.e., two sources are indistinguishable if the distance between them is smaller than one-half of the predominant wavelength). Reduced event-location errors can be expected from WI because it operates with waveforms and

includes multiples, scattered waves, etc. Another potential benefit of WI, not explored in this paper, is an improved accuracy of the velocity model.

Employing the approach described in Kim et al. (2011), Jarillo Michel and Tsvankin (2014) implement WI gradient calculation for the source location and moment tensor of a microseismic event in a 2D VTI medium. Their results, based on the adjoint-state method, show that the adjoint wavefield can also help identify the presence of missed sources and, in general, improve the initial source position for WI.

Here, we present a methodology for estimating the parameters $\mathbf{x}^s$, t_0, and $\mathbf{M}$ using 2D waveform inversion. First, calculation of the gradient of the objective function is implemented for dislocation-type sources embedded in heterogeneous VTI media using the adjoint-state method (Jarillo Michel and Tsvankin, 2014). Multicomponent wavefields for forward and adjoint computations are generated with a 2D elastic finite-difference algorithm. Then we introduce an iterative local gradient-descent algorithm for simultaneous updating of all source parameters. The inversion involves the so-called nondimensionalization approach (Kim et al., 2011) because the model parameters belong to different classes (i.e., have different units). Finally, the methodology is tested on multicomponent data from horizontally layered VTI media.

FORWARD PROBLEM FOR MICROSEISMIC DATA

The wave equation for a dislocation-type source embedded in a heterogeneous anisotropic medium can be written as:

$$\rho(\partial^2 u_i/\partial t^2) - \partial[c_{ijkl}(\partial u_k/\partial x_l)]/\partial x_j = -M_{ij}\{\partial[\delta(\mathbf{x} - \mathbf{x}^S)]/\partial x_j\} S(t) , \quad (1)$$

where $\mathbf{u}(\mathbf{x},t)$ is the displacement field, t is time, c_{ijkl} is the stiffness tensor (i,j,k,l = 1,2,3), $\rho(\mathbf{x})$ is density, $\mathbf{M}$ is the seismic moment tensor, $\mathbf{x}^S$ is the source location, S(t) is the source time function, and $\delta(\mathbf{x} - \mathbf{x}^S)$ is the spatial δ-function. The moment tensor $\mathbf{M}$ is incorporated into eq. (1) by using the notion of equivalent force (Aki and Richards, 2002; Dahlen and Tromp, 1998; Jost and Herrmann, 1989). Summation over repeated indices is implied.

The elastic finite-difference (FD) code `sfewe` in `MADAGASCAR` is employed to obtain solutions of eq. (1) for VTI media. The code generates only the in-plane polarized (P and SV) modes, which are described here by the Thomsen (1986) parameters - the P- and S-wave vertical velocities V_{P0} and V_{S0} and the anisotropy coefficients ε and δ (the coefficient γ influences SH-waves only). The kinematic signatures of SV-waves are mostly governed by the combination of Thomsen parameters denoted as $\sigma \equiv (V_{P0}/V_{S0})^2(\varepsilon - \delta)$ (Tsvankin, 2012).

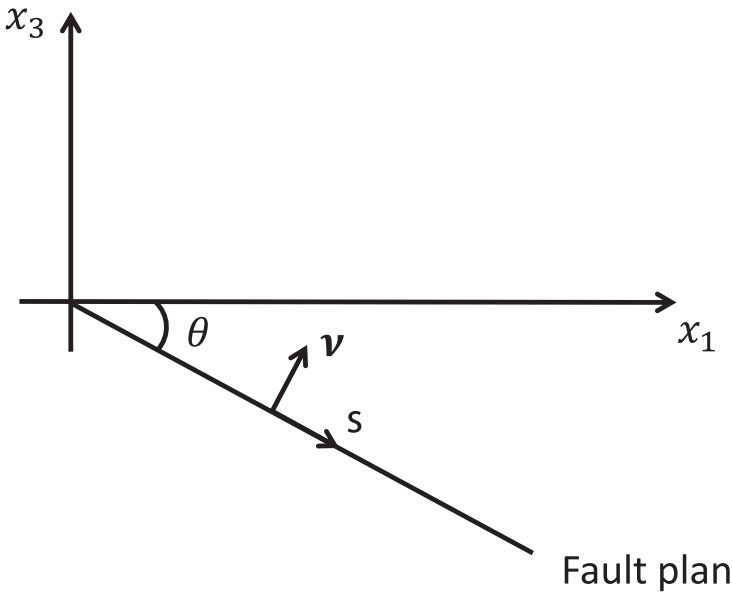

Fig. 1. 2D fault geometry used in forward modeling. The dip angle θ ($0° \le \theta \le 90°$) is measured down from the horizontal axis. The incidence plane $[x_1;x_3]$ is assumed to coincide with the dip plane of the fault and contain the slip vector **s**.

The relevant elements of the moment tensor M of a dislocation-type source for the in-plane polarized waves in a VTI medium can be represented as (Aki and Richards, 2002; Vavryčuk, 2005; Jarillo Michel and Tsvankin, 2014):

$$M_{11} = -[(\Sigma\bar{u})/2] \sin 2\theta\, (c_{13} - c_{11}) , \tag{2}$$

$$M_{13} = M_{31} = \Sigma\bar{u} \cos 2\theta\, c_{55} , \tag{3}$$

$$M_{33} = -[(\Sigma\bar{u})/2] \sin 2\theta\, (c_{33} - c_{13}) , \tag{4}$$

where Σ is the fault area, $\bar{u}$ is the magnitude of the slip (displacement discontinuity), and c_{11}, c_{13}, c_{33}, and c_{55} are the stiffness coefficients in the two-index Voigt notation (Fig. 1).

Typical wavefields generated by a dislocation-type source in a layered VTI medium (Fig. 2) are shown in Fig. 3. The P-wavefront is visibly extended in the horizontal direction because the parameter $\varepsilon = 0.4$ is positive and relatively large. The amplitude distribution and intensity of the P- and S-waves change substantially with the fault orientation. The wavefront of the SV-mode triplicates and becomes multivalued due to the large value of σ in the source layer (Tsvankin, 2012).

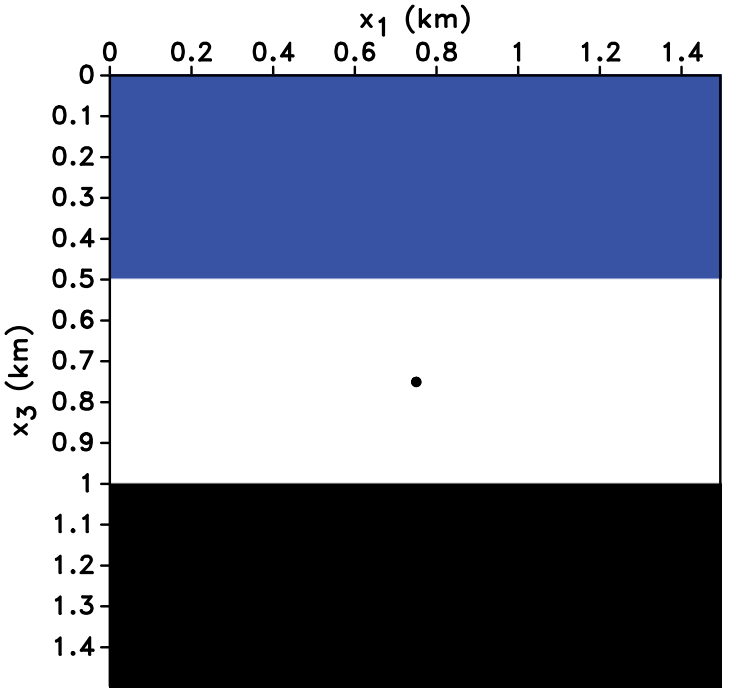

Fig. 2. Three-layer VTI model used in the modeling experiment. The parameters $\rho = 2$ kg/m^3, $\varepsilon = 0.4$, and $\delta = 0$ are the same in all three layers. The vertical velocities in the top layer are $V_{P0} = 4047$ m/s and $V_{S0} = 2638$ m/s; for the second layer, $V_{P0} = 4169$ m/s and $V_{S0} = 2320$ m/s; for the third layer, $V_{P0} = 4693$ m/s and $V_{S0} = 2682$ m/s. The source (black dot) is located in the middle layer.

INVERSION METHODOLOGY

Our goal is to estimate the source coordinates x_1^S and x_3^S, the origin time t_0, and moment-tensor elements M_{11}, M_{13}, and M_{33} assuming that the velocity model is known. Hence, the vector of unknown model parameters is defined as:

$$\mathbf{m} = \{x_1^S, x_3^S, t_0, M_{11}, M_{13}, M_{33}\} . \tag{5}$$

The data residuals are measured by the least-squares objective function F, which is minimized by the inversion algorithm:

$$F(\mathbf{m}) = \tfrac{1}{2} \| \mathbf{d}_{pre}(\mathbf{m}) - \mathbf{d}_{obs} \|^2 , \tag{6}$$

where $\mathbf{d}_{obs}$ is the observed displacement and $\mathbf{d}_{pre}(\mathbf{m})$ is the predicted displacement. Both $\mathbf{d}_{obs}$ and $\mathbf{d}_{pre}$ are generated by the FD code mentioned above, with the wavefield excited by a single source at $\mathbf{x}^S$ and recorded by N receivers located at $\mathbf{x}^{r_n}$ (n = 1,2,...,N).

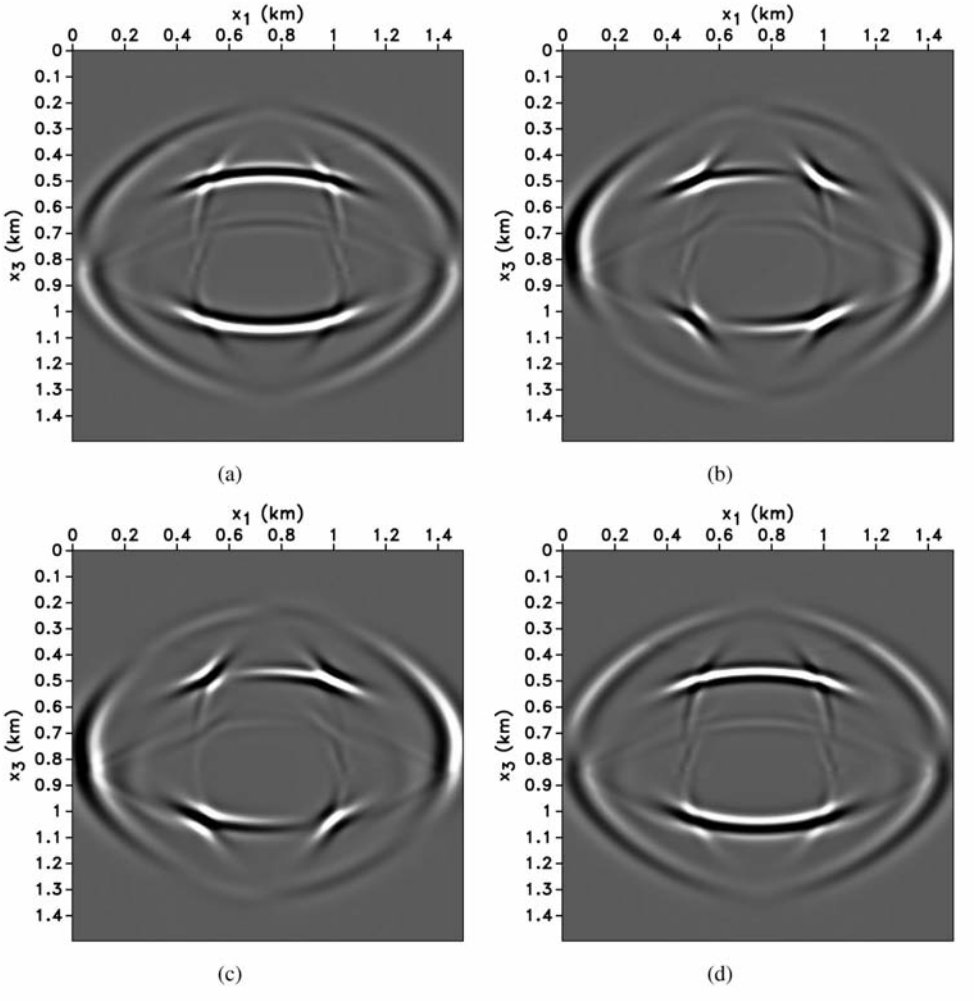

Fig. 3. Horizontal displacement generated by a dip-slip source with different orientation (defined by the angle θ, see Fig. 1) in the VTI medium from Fig. 2. The moment tensor is computed from eqs. (2) - (4) with $\Sigma \underline{u} = 1$ m^3 and (a) $\theta = 0°$, (b) $\theta = 30°$, (c) $\theta = 60°$, and (d) $\theta = 90°$.

Application of the adjoint-state method

The adjoint-state method is designed to efficiently calculate the derivatives of the objective function with respect to the model parameters, $\partial F(\mathbf{m})/\partial \mathbf{m}$. Computation of the gradient of the objective function for our problem is discussed in Jarillo Michel and Tsvankin (2014).

The derivatives of the objective function with respect to the source coordinates, origin time, and moment-tensor elements can be found as (Kim et al., 2011; Jarillo Michel and Tsvankin, 2014):

$$g_{x_i^s} = \partial F/\partial x_i^s = \int_0^T \partial[\mathbf{M}:\boldsymbol{\varepsilon}^\dagger(\mathbf{x}^{ts},t)]/\partial x_i|_{\mathbf{x}^{ts}} S(T - t)\, dt , \quad (7)$$

$$g_{t_0} = \partial F/\partial t_0 = \int_0^T \mathbf{M}:\boldsymbol{\varepsilon}^\dagger(\mathbf{x}^{ts},t)\, [\partial S(T - t)/\partial t]\, dt , \quad (8)$$

$$g_{M_{ij}} = \partial F/\partial M_{ij} = \int_0^T \varepsilon_{ij}^\dagger(\mathbf{x}^{ts},t)\, S(T - t)\, dt , \quad (9)$$

where $\mathbf{x}^{ts}$ is the trial source location, T is the recording time, $\boldsymbol{\varepsilon}^\dagger = \frac{1}{2}[\nabla\mathbf{u}^\dagger + (\nabla\mathbf{u}^\dagger)^T]$ is the adjoint strain tensor, and $\mathbf{M}:\boldsymbol{\varepsilon}^\dagger$ is the double inner product of the tensors $\mathbf{M}$ and $\boldsymbol{\varepsilon}^\dagger$. Eqs. (7) - (9) applied to the 2D problem at hand yield the gradient vector $\mathbf{g}$ for the six source parameters:

$$\mathbf{g} = \{\partial F/\partial x_1^s,\ \partial F/\partial x_3^s,\ \partial F/\partial t_0,\ \partial F/\partial M_{11},\ \partial F/\partial M_{13},\ \partial F/\partial M_{33}\} . \quad (10)$$

For inversion purposes, the derivatives in eqs. (7) - (9) are needed only at the trial source position. The derivatives for $\mathbf{x}^s$ and t_0 [eqs. (7) and (8)] include the double-inner product $\mathbf{M}:\boldsymbol{\varepsilon}^\dagger(\mathbf{x}^{ts}, t)$, which involves summation over all elements of $\mathbf{M}$. Hence, stable inversion for $\mathbf{x}^s$ and t_0 requires an accurate initial model for the moment tensor.

Nondimensionalization of the model parameters

The model parameters have different units, and local minimization of $F(\mathbf{m})$ could be performed for each parameter class separately. However, here we carry out simultaneous inversion for $\mathbf{x}^s$, t_0, and $\mathbf{M}$ employing the nondimensionalization approach suggested by Kim et al. (2011), which also helps avoid the additional computational cost of multidirectional minimization. This approach eliminates the difference between the units of different parameters classes, which makes possible simultaneous parameter updating. At the first iteration, we define the following scaling coefficients σ for the three classes of parameters:

$$\sigma_{\mathbf{x}^s} = \beta_{\mathbf{x}^s}\, [1/\sqrt{(g_{x_1^s}^2 + g_{x_3^s}^2)}] , \quad (11)$$

$$\sigma_{t_0} = \beta_{t_0}\, (1/|g_{t_0}|) , \quad (12)$$

$$\sigma_{\mathbf{M}} = \beta_{\mathbf{M}}\, [1/\sqrt{(g_{M_{11}}^2 + g_{M_{13}}^2 + g_{M_{33}}^2)}] , \quad (13)$$

where the factors β , β_M, and β ensure that each parameter class gives a comparable contribution to the gradient. These factors may be different for each experiment and can be determined, for instance, by evaluating the change in the gradient produced by β_c (c indicates the parameter class) between the first and second iteration. The "nondimensionalized" model parameters are:

$$\hat{\mathbf{m}}_c = \mathbf{m}_c/\sigma_c \ . \tag{14}$$

The gradient becomes dimensionless after the following scaling:

$$\hat{\mathbf{g}}_c = \mathbf{g}_c \sigma_c \ . \tag{15}$$

Model-updating algorithm

As discussed in more detail below, the inverse problem is nonlinear, and we solve it using an iterative local gradient-descent scheme. Suppose the model $\mathbf{m}^k$ is obtained after $k-1$ iterations of the inversion algorithm. First, the forward simulation is performed to generate the predicted data $\mathbf{d}^k_{pre}(\mathbf{m}^k)$, which allows us to compute the objective function F^k. Then, we carry out the adjoint simulation to calculate the gradient $\mathbf{g}^k$ using eqs. (7) - (9). The next step is nondimensionalization of the model parameters [eq. (14)] and scaling of the gradient [eq. (15)]. Note that the scaling coefficients are computed at the first iteration and kept constant during the inversion. Because the nondimensionalized model parameters have the same units (those of F) and the scaled gradient is dimensionless, the three classes of parameters can be updated simultaneously using a step length α:

$$\hat{\mathbf{m}}_{k+1} = \hat{\mathbf{m}}_k + \alpha \hat{\mathbf{g}}_k \ . \tag{16}$$

In principle, α can be computed from line-search algorithms discussed by Gauthier et al. (1986), Virieux and Operto (2009), and Pratt (2013). However, their accuracy is limited by the parameters used in numerical modeling. In particular, line search cannot be used to update the source location within a distance smaller than the grid spacing. Here, we employ a constant step length, which does not have this problem.

Assuming that $\hat{\mathbf{m}}_k$ is located within the basin that contains the global minimum of F, the step length should be sufficiently small to ensure that $\hat{\mathbf{m}}_{k+1}$ stays within this basin. After the update, the parameters have to be "dimensionalized" again so that they can be used as inputs for the forward modeling in the next iteration:

$$\mathbf{m}_c^{k+1} = \hat{\mathbf{m}}_c^{k+1} \sigma_c \ . \tag{17}$$

Properties of the inverse problem

Estimating the moment tensor **M** of an earthquake from seismic amplitudes is a linear inverse problem. However, simultaneous inversion for **M**, $\mathbf{x}^s$, and t_0 is nonlinear because the recorded data depend on $\mathbf{x}^s$ and t_0 in a nonlinear fashion. The joint inversion for **M**, $\mathbf{x}^s$, and t_0 involves complications, which are also typical for velocity estimation using WI. For example, cycle-skipping can occur if the trial model is too far from the actual one or if the step length α used in model updating is too large. In particular, the trial source should be within about one-half of the predominant wavelength from the actual source location.

Fig. 4 shows the variation of the normalized objective function with the coordinates $\mathbf{x}^s$ and time t_0. To ensure convergence to the actual values, the trial model should lie within the basin that contains the global minimum. If the inversion involves simultaneous estimation of x_1^s, x_3^s, and t_0, the basin containing the global minimum in the plots of Fig. 4 becomes more narrow, which increases the risk of cycle skipping.

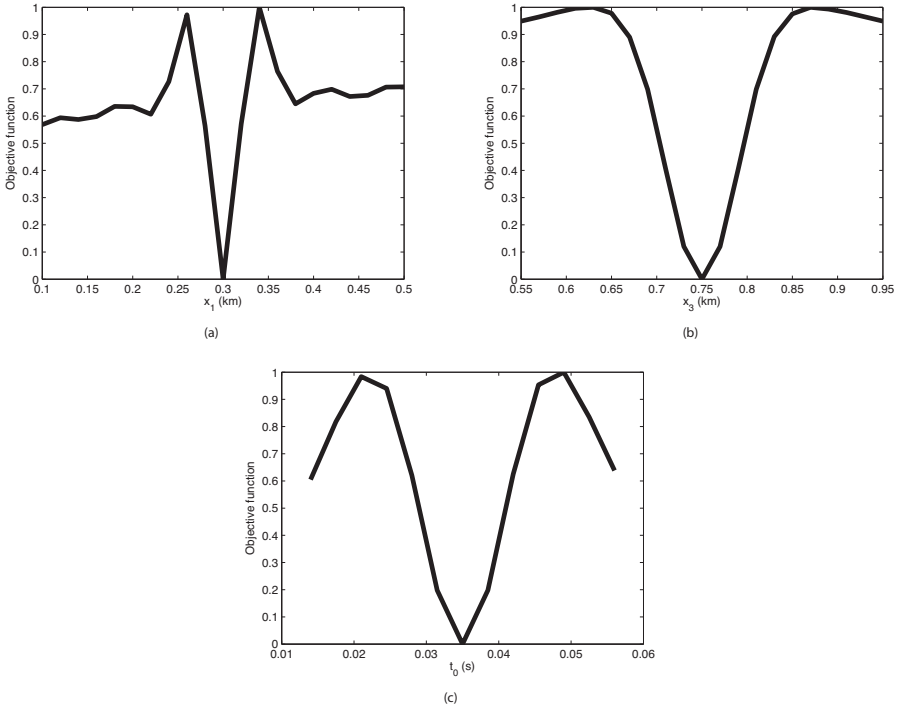

Fig. 4. Dependence of the objective function $F(\mathbf{m})$ on the trial source parameters (a) x_1^s, (b) x_3^s, and (c) t_0 for a homogeneous VTI model. The global minimum coincides with the actual parameter value. In each test the other parameters are fixed at the actual values. The medium parameters are V_{P0} = 4047 m/s, V_{S0} = 2638 m/s, ρ = 2 g/cm^3, ε = 0.4, and δ = 0.

SYNTHETIC TESTS

Here, we present synthetic tests of the WI algorithm for a homogeneous VTI medium and a stack of horizontal VTI layers. In all experiments, the observed data are generated by a single microseismic event recorded by a vertical array of closely spaced receivers.

In the first test, we invert for the parameters x_1^s, x_3^s, M_{11}, M_{13}, and M_{33} with the origin time t_0 fixed at the actual value (Fig. 5). Because the medium is homogeneous, the wavefield is composed of just the direct P- and SV-waves. The objective function becomes practically negligible after about 10 iterations (Fig. 6). The source coordinates (Fig. 7) and moment tensor (Fig. 8) are estimated with high accuracy; the errors in x_1^s and x_3^s are on the order of centimeters. Note that the algorithm was able to resolve the moment tensor **M**, although the data were acquired in a single vertical borehole. The pronounced variations in **M** during the initial iterations are due to the incorrect position of the source, which produces large changes in the amplitudes of the P- and SV-waves.

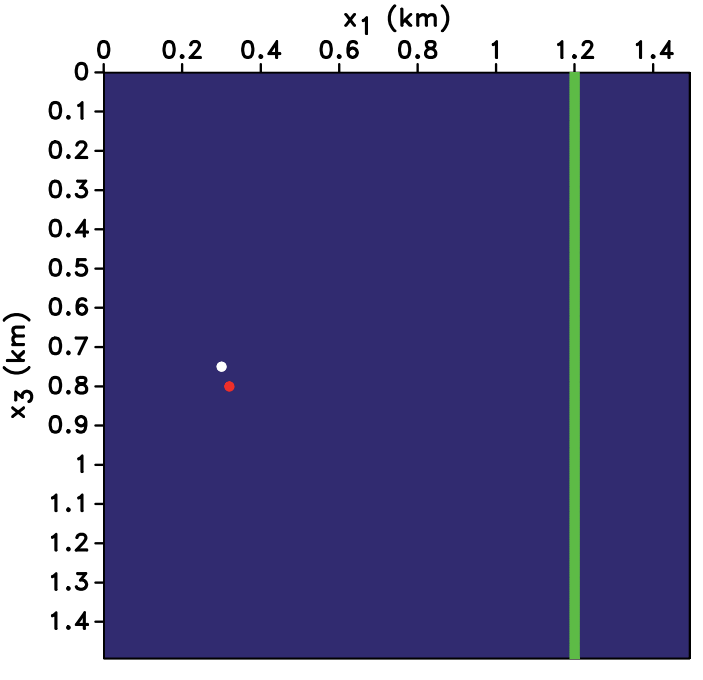

Fig. 5. Actual source (white dot), trial source (grey dot) and a vertical line of receivers (spacing is 6 m) embedded in a homogeneous VTI medium. The medium parameters are V_{P0} = 4047 m/s, V_{S0} = 2638 m/s, ρ = 2 g/cm^3, ε = 0.4, and δ = 0. The actual source is located at x_1 = 0.3 km and x_3 = 0.75 km with θ = 0° [see eqs. (2)-(4)]. For the trial source, x_1 = 0.32 km, x_3 = 0.8 km, and θ = 15°. Both the actual and trial sources are set off at the same time (t_0 = 0.049 s) and have the same $\Sigma\bar{u}$ = 1 m^3.

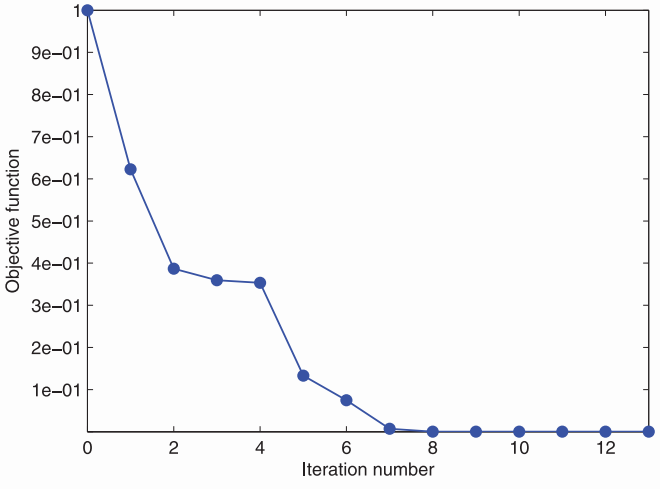

Fig. 6. Change of the normalized objective function $F(\mathbf{m})$ with iterations for the model in Fig. 5.

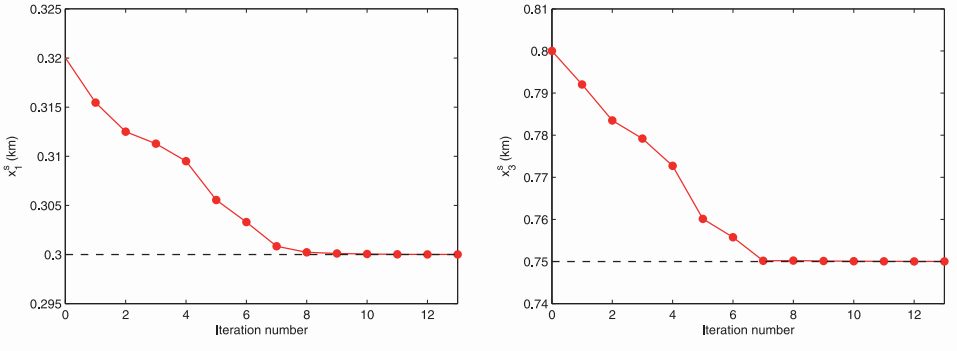

(a) (b)

Fig. 7. Change of the source coordinates (a) x_1^s and (b) x_3^s with iterations for the model in Fig. 5. The actual values are marked by dashed lines.

In the next experiment we use a more realistic VTI model (Fig. 9) and assume that all source parameters ($\mathbf{x}^s$, t_0, and $\mathbf{M}$) are unknown. The multiple interfaces in this model produce numerous scattered waves, which should help constrain the source location. Although the origin time t_0 for the actual and trial sources coincides, it varies with iterations as WI tries to match the observed and predicted data. Apart from small errors in $\mathbf{x}^s$ and t_0, caused by the tradeoff between the origin time and source location, the inversion results are accurate (Figs. 11 and 12).

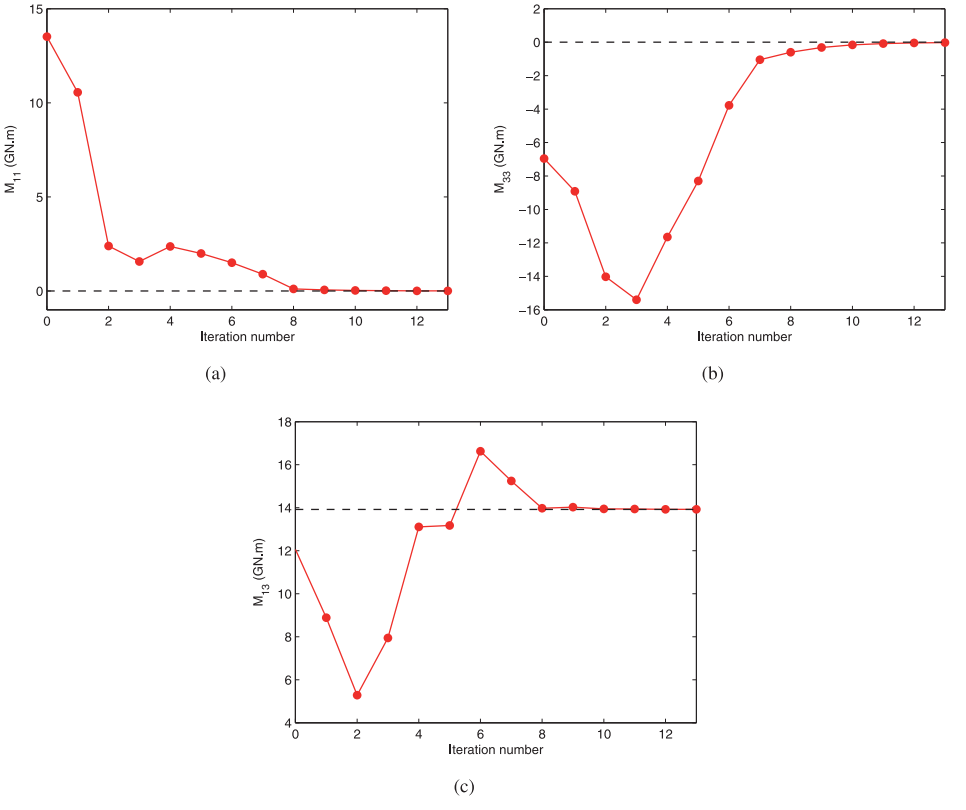

Fig. 8. Change of the moment-tensor elements (a) M_{11}, (b) M_{33}, and (c) M_{13} with iterations for the model in Fig. 5. The actual values are marked by dashed lines.

In principle, the parameters $\mathbf{x}^s$ and t_0 influence the traveltimes in a different way, which should preclude a trade-off between them. Indeed, moving the source vertically shifts the apex of the P- and S-wave moveouts up or down, with the depth of the apex determining the vertical coordinate x_3^s. Also, variations in the horizontal distance between the source and the receiver array change the difference between the S- and P-wave traveltimes. In contrast, changing the origin time simply shifts the P- and S-wave moveouts along the time axis without moving them in depth or altering their difference. However, P- and SV-traveltime shifts produced by perturbations in the source location and origin time near the global minimum of the objective function become too small to rapidly guide the inversion toward the actual model.

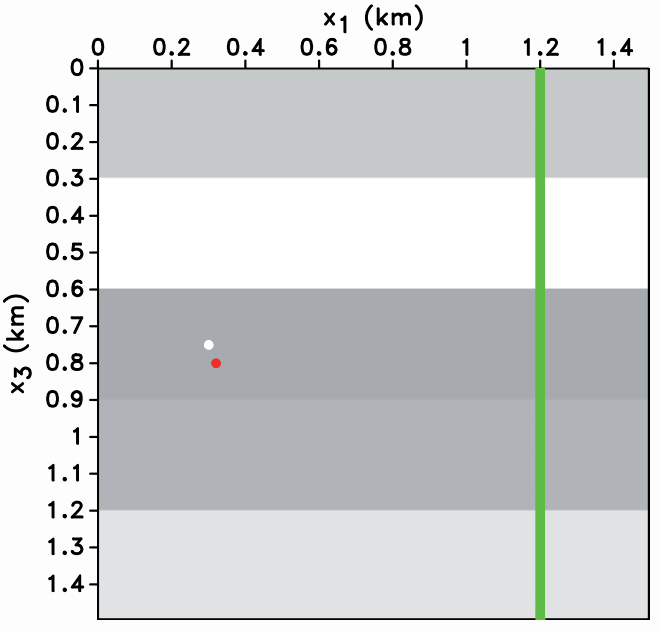

Fig. 9. Actual (white dot) and trial (grey dot) sources and a vertical receiver array in a five-layer VTI model. The receiver geometry is the same as in Fig. 5. The parameters $\rho = 2$ kg/m^3, $\varepsilon = 0.4$, and $\delta = 0$ are the same in all five layers. The vertical velocities in the top layer are $V_{P0} = 4419$ m/s and $V_{S0} = 2645$ m/s; for the second layer, $V_{P0} = 4956$ m/s and $V_{S0} = 2424$ m/s; for the third layer, $V_{P0} = 4048$ m/s and $V_{S0} = 2638$ m/s; for the fourth layer, $V_{P0} = 4170$ m/s and $V_{S0} = 2320$ m/s; for the fifth layer, $V_{P0} = 4694$ m/s and $V_{S0} = 2682$ m/s. The actual source is located at $x_1 = 0.3$ km and $x_3 = 0.75$ km with $\theta = 0°$. The trial source is located at $x_1 = 0.3$ km and $x_3 = 0.8$ km with $\theta = 15°$. Both events occur at the same time ($t_0 = 0.035$ s) and have the same $\Sigma u = 1$ m^3.

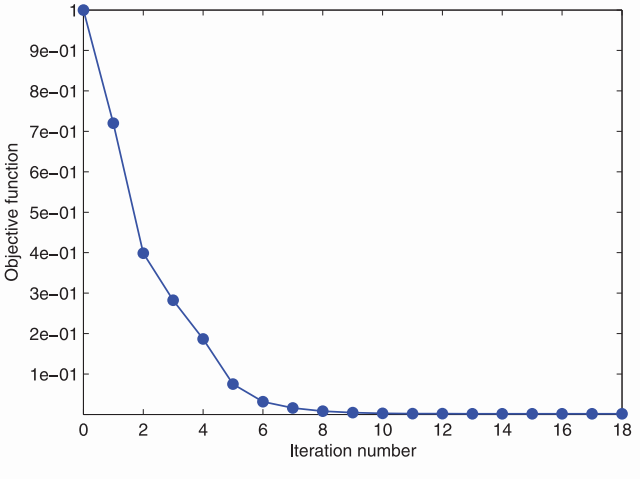

Fig. 10. Change of the normalized objective function $F(\mathbf{m})$ with iterations for the model in Fig. 9. All source parameters are unknown.

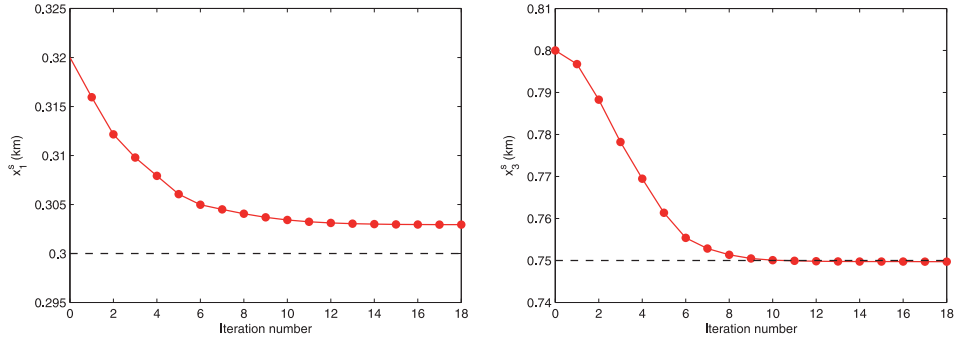

Fig. 11. Change of the source coordinates (a) x_1^s and (b) x_3^s with iterations for the model in Fig. 9.

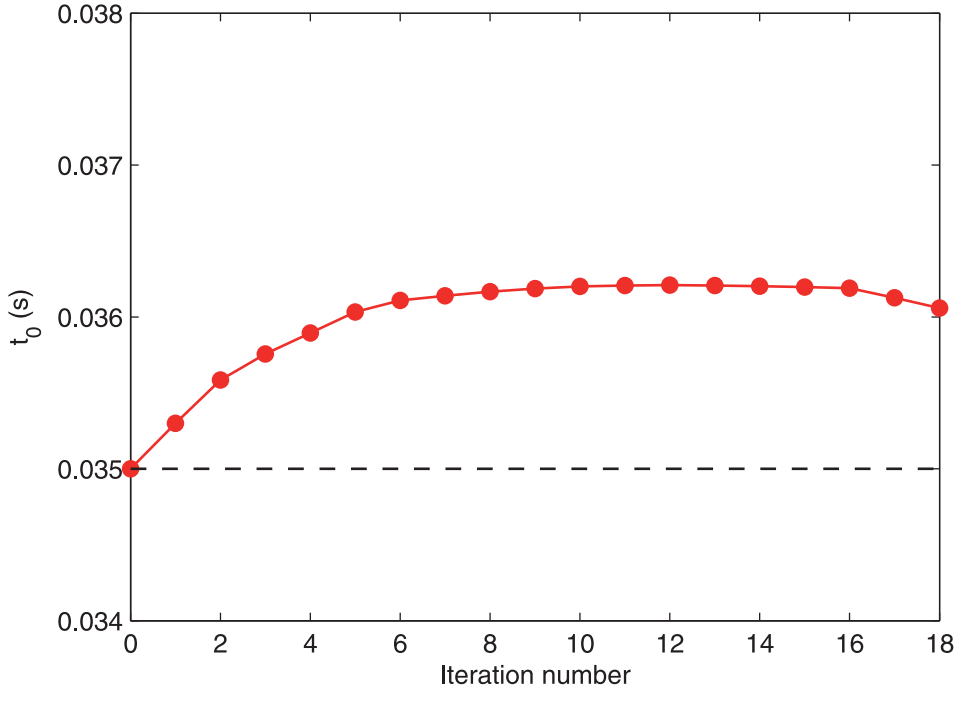

Fig. 12. Change of the origin time t_0 with iterations for the model in Fig. 9.

The previous tests assumed the correct velocity model for WI. The next example helps evaluate the influence of velocity errors on the inversion results by using a distorted anisotropy coefficient ε for the homogeneous VTI model in Fig. 5. The algorithm estimates the parameters $\mathbf{x}^s$ and $\mathbf{M}$, whereas the origin time t_0 is fixed at the actual value. In particular, an error in ε changes the P-wave horizontal velocity V_{hor}, which should influence estimation of the horizontal source coordinate x_1^s. After a fast initial decrease, the objective function flattens out (Fig. 13) at a larger value than that in Fig. 6. Still, errors in the source coordinates are relatively small (about 5 m for x_1^s) and the elements M_{11} and M_{33} of the moment tensor are also recovered with high accuracy (Figs. 14 and 15). However, there is a more significant error (over 20%) in the element M_{13}, which is most sensitive to the quality of waveform matching.

The goal of the final test is to evaluate the influence of noise in the input data on the inversion results. We use the homogeneous VTI model from Fig. 5 and add substantial random Gaussian noise in the frequency band of the observed data. The noise does not completely mask the arrivals but creates significant distortions in the seismogram (Fig. 16). The inversion algorithm estimates $\mathbf{x}^s$ and $\mathbf{M}$ (t_0 is fixed at the actual value); the results of this test with noise-free data are shown in Figs. 6 - 8. The objective function (Fig. 17) is not monotonic and flattens out at a larger value than that in Fig. 6, as expected for noise-contaminated data.

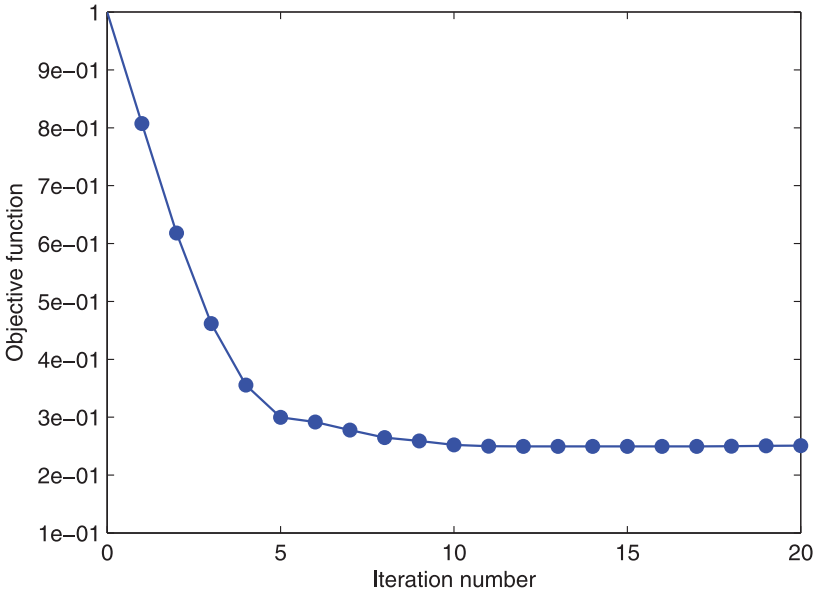

Fig. 13. Change of the normalized objective function $F(\mathbf{m})$ with iterations for the model in Fig. 5. The inversion is performed with an incorrect value of ε ($\varepsilon = 0.3$ instead of the actual 0.4). The rest of the VTI parameters are unchanged.

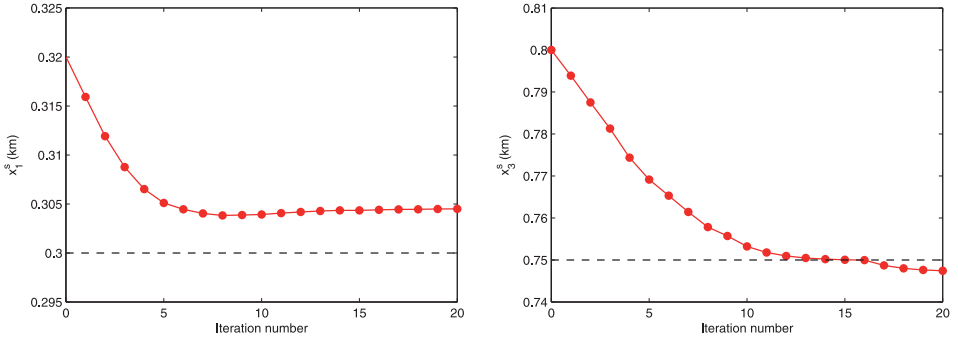

Fig. 14. Change of the source coordinates (a) x_1^s and (b) x_3^s with iterations for the model in Fig. 5. The inversion uses $\varepsilon = 0.3$ instead of the actual $\varepsilon = 0.4$.

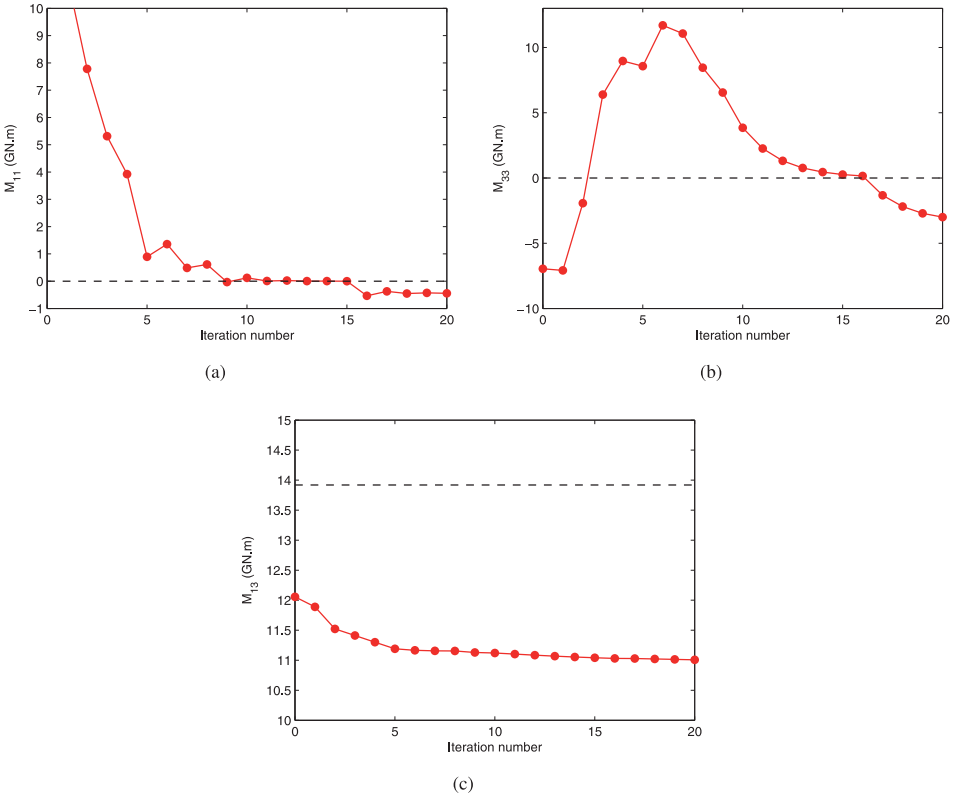

Fig. 15. Change of the moment-tensor elements (a) M_{11}, (b) M_{33}, and (c) M_{13} with iterations for the model in Fig. 5. The inversion uses $\varepsilon = 0.3$ instead of the actual $\varepsilon = 0.4$.

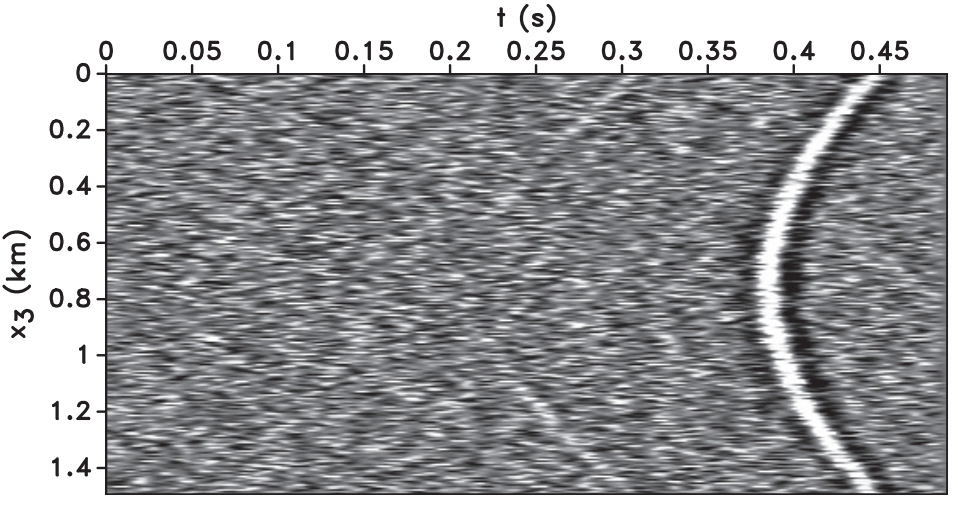

Fig. 16. Vertical displacement of the observed data contaminated with Gaussian noise for the model in Fig. 5. The noise has the same frequency band as the data and the signal-to-noise ratio is 1.5.

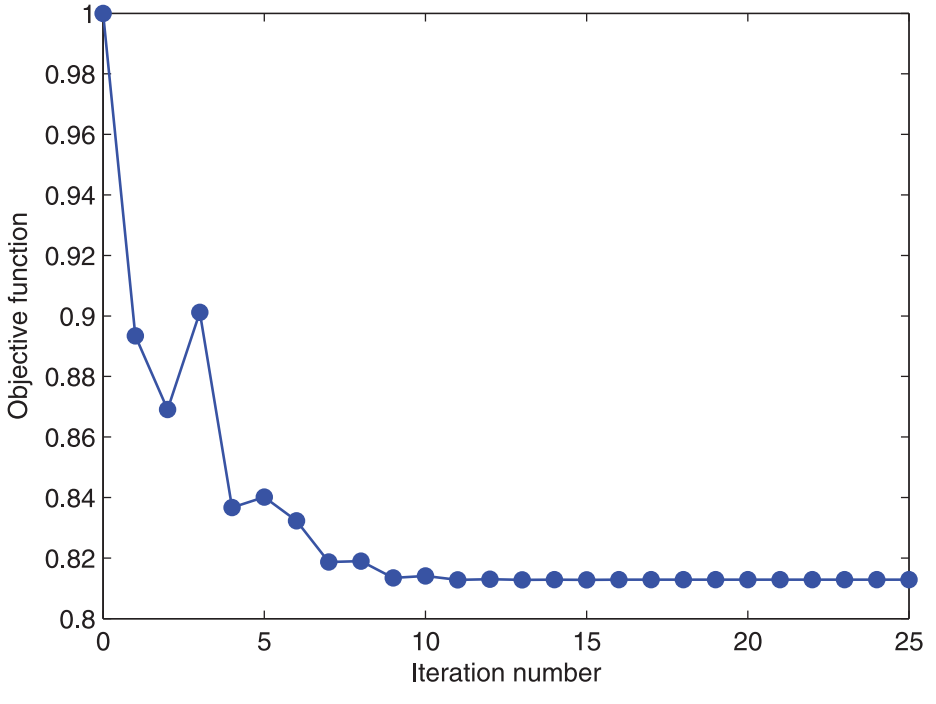

Fig. 17. Change of the normalized objective function $F(\mathbf{m})$ with iterations for the model in Fig. 5. The inversion was performed on noise-contaminated data (see Fig. 16).

Still, despite the substantial magnitude of noise, the errors in the estimated source coordinates (Fig. 18) and the elements of the tensor **M** (Fig. 19) are relatively small. Because the noise influences primarily the amplitudes, one would expect it to distort mostly the tensor **M**. However, as discussed above, the gradient for the source coordinates $\mathbf{x}^s$ depends on M, which causes small errors in x_1^s and x_3^s (Fig. 18). The only noticeably distorted parameter is the tensor element M_{13}, for which the error is about 16%. For the tested VTI models, the variance of Gaussian noise has to reach 20% of the maximum amplitude for the search to get trapped in local minima.

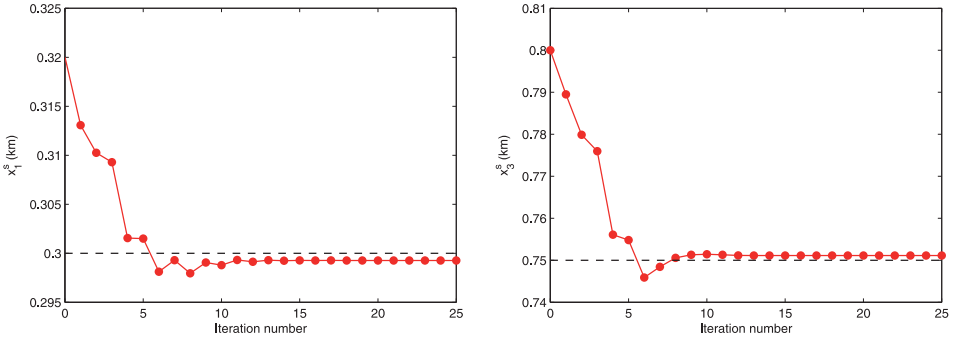

Fig. 18. Change of the source coordinates (a) x_1^s and (b) x_3^s with iterations for the model in Fig. 5. The inversion was performed on noise-contaminated data (see Fig. 16).

DISCUSSION

The results presented here are limited to 2D VTI models, although the developed methodology can be applied to 3D data from lower-symmetry media. Seismograms recorded in the field are influenced by such factors as attenuation and velocity dispersion, which are not accounted for in the forward-modeling code employed here. Also, amplitude matching for field data would require 2.5D corrections of the geometric spreading. Although the current version of the algorithm is designed for VTI models, it can be applied to vertical symmetry planes of orthorhombic media with an appropriate geometric-spreading correction. However, inclusion of out-of-plane azimuths requires 3D modeling capable of simulating the fast and slow S-waves rather than just the SV-mode. Extension of the algorithm to 3D anisotropic models is part of the ongoing work on the project.

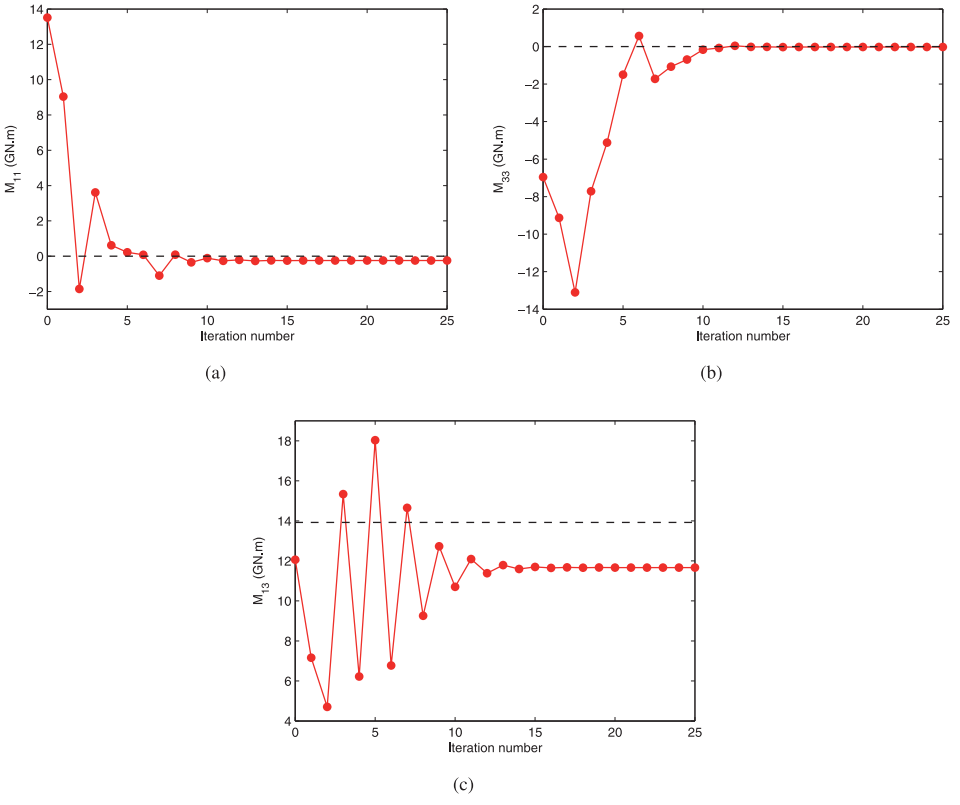

Fig. 19. Change of the moment-tensor elements (a) M_{11}, (b) M_{33}, and (c) M_{13} with iterations for the model in Fig. 5. The inversion was performed on noise-contaminated data (see Fig. 16).

Even if the incidence plane represents a plane of symmetry, the wavefield contains the SH-mode, which is not generated by our FD code. Inclusion of SH-waves can help better constrain the model parameters and estimate the moment-tensor elements M_{12} and M_{23} (Vavryčuk, 2007) for single-well geometry. In general, the inversion using receiver arrays in several wells should be highly beneficial for both event location and recovery of the moment tensor.

Although the VTI velocity model was assumed known, the adjoint-state method is capable of calculating the gradient for the source and velocity parameters simultaneously. The updating procedure that includes the velocity field takes only two modeling simulations and does not substantially increase the computational cost. Hence, to take full advantage of the adjoint-state method and WI in microseismic monitoring, our methodology could be extended to

anisotropic velocity model building. As is done in kinematic inversion, event location can be performed simultaneously with anisotropic parameter estimation, although this approach may result in model-dependent trade-offs. A careful study of such trade-offs should provide a better understanding of the potential of WI in microseismic studies.

CONCLUSIONS

Waveform inversion is a potentially powerful tool to solve simultaneously two of the most important problems in microseismic monitoring, event location and source-mechanism estimation. The WI algorithm presented here operates with the elastic wave equation for 2D heterogeneous VTI media. In addition to employing the waveforms (potentially, for the entire trace), the WI method simultaneously inverts for the parameters that are typically obtained separately by kinematic and amplitude techniques. The gradient for the source parameters (location $\mathbf{x}^s$, origin time t_0, and moment tensor $\mathbf{M}$) was computed using the adjoint-state method. The nondimensionalization approach was applied to handle model updating for different parameter classes.

Synthetic tests were performed for data recorded by a dense vertical array of two-component receivers in homogeneous and horizontally layered VTI media. Increasing the number of layers is generally beneficial for our algorithm (provided the velocity model is accurate) because multiple reflections and conversions improve the sensitivity of WI to the source parameters. If the initial model is located within the basin of convergence, WI accurately estimates the parameters $\mathbf{x}^s$, t_0, and $\mathbf{M}$, especially when the origin time is fixed at the correct value. Although in theory there is no trade-off between the source location and origin time, the traveltime differences responsible for resolving $\mathbf{x}^s$ and t_0 are small near the global minimum. As a result, simultaneous inversion for the source coordinates and origin time may lead to small distortions in x_1^s and t_0.

The algorithm can tolerate moderate errors in the velocity model, which was illustrated by estimating the parameters of a source in a homogeneous VTI medium using an inaccurate anisotropy coefficient ε (0.3 instead of 0.4). Predictably, a distortion in ε propagates into the horizontal source coordinate, but the errors in x_1^s and other parameters are not significant. The only exception is the moment-tensor element M_{13}, which is most sensitive to waveform matching.

To assess the stability of the algorithm, the input data were contaminated with Gaussian noise in the frequency band of the observed data and the signal-to-noise ratio is 1.5. Although the arrivals are partially masked by noise and the objective function is not reduced as much as in other tests, the only noticeably distorted parameter is M_{13}.

ACKNOWLEDGMENTS

We are grateful to Vladimir Grechka (Marathon Oil), who generously provided valuable insights and feedback regarding various aspects of this work. We thank Esteban Díaz Pantin and Nishant Kamath (both from CWP) for their technical assistance with the inversion algorithm and Gerhard Pratt (University of Western Ontario) for his advice on waveform inversion. The numerical examples in this paper are produced with the MADAGASCAR open-source software package freely available at www.ahay.org. This work was supported by the Consortium Project on Seismic Inverse Methods for Complex Structures at the Center for Wave Phenomena (CWP).

REFERENCES

Aki, K., and Richards, P.G., 2002. Quantitative Seismology. University Science Books, Mill Valley, CA.

Dahlen, F.A. and Tromp, J., 1998. Theoretical Global Seismology. Princeton University Press, Princeton, NJ.

Fichtner, A., 2006. The adjoint method in seismology: I. Theory. Phys. Earth Planet. Inter., 157: 86-104.

Fichtner, A., 2009. Full Seismic Waveform Inversion for Structural and Source Parameters. Ph.D. thesis, Ludwig-Maximilians-University, München.

Gauthier, O., Virieux, J. and Tarantola, A., 1986. Two-dimensional nonlinear inversion of seismic waveforms: Numerical results. Geophysics, 51: 1387-1403.

Grechka, V., Singh, P. and Das, I., 2011. Estimation of effective anisotropy simultaneously with locations of microseismic events. Geophysics, 76: WC143-WC155.

Grechka, V. and Yaskevich, S., 2013. Azimuthal anisotropy in microseismic monitoring: Part 1 Theory. Expanded Abstr., 83rd Ann. Internat. SEG Mtg., Houston: 1987-1991.

Grechka, V. and Yaskevich, S., 2014. Azimuthal anisotropy in microseismic monitoring: A Bakken case study. Geophysics, 79: KS1-KS12.

Jarillo Michel, O. and Tsvankin, I., 2014. Gradient calculation for waveform inversion of microseismic data in VTI media. J. Seismic Explor., 23: 201-217.

Jost, M.L. and Herrmann, R.B., 1989. A students guide to and review of moment tensors. Seismol. Res. Lett., 60: 37-57.

Kamath, N. and Tsvankin, I., 2013. Full-waveform inversion of multicomponent data for horizontally layered VTI media. Geophysics, 78: WC113-WC121.

Kendall, M., Maxwell, S., Foulger, G., Eisner, L. and Lawrence, Z., 2011. Microseismicity: Beyond dots in a box. Introduction. Geophysics, 76: WC1-WC3.

Kim, Y., Liu, Q. and Tromp, J., 2011. Adjoint centroid-moment tensor inversions. Geophys. J. Internat., 186: 264-278.

Lailly, P., 1983. The seismic inverse problem as a sequence of before stack migrations. In: Bednar, J.B., Redner, R., Robinson, E. and Weglein, A., Eds., Conf. Inverse Scattering: Theory and Application. Soc. Industr. Appl. Math.: 206-220.

Lee, H.-Y., Koo, J.M. Min, D.-J. Kwon, B.-J. and Yoo, H.S., 2010. Frequency-domain elastic full waveform inversion for VTI media. Geophys. J. Internat., 183: 884-904.

Li, J., Toksöz, M.N., Li, C., Morton, S., Dohmen, T. and Katahara, K., 2013. Locating Bakken microseismic events with simultaneous anisotropic tomography and extended double-difference method. Expanded Abstr., 83rd Ann. Internat. SEG Mtg., Houston: 2073-2078.

Lions, J., 1972. Nonhomogeneous Boundary Value Problems and Applications. Springer Verlag, Berlin.

Liu, Q. and Tromp, J., 2006. Finite-frequency kernels based on adjoint methods. Bull. Seismol. Soc. Am., 96: 2383-2397.

Maxwell, S., 2010, Microseismic: Growth born from success. The Leading Edge, 29: 338-343.

Morency, C. and Mellors, R.J., 2012. Full moment tensor and source location inversion based on full waveform adjoint inversion: application at the Geysers geothermal field. Expanded Abstr., 82nd Ann. Internat SEG Mtg., Las Vegas, 532: 1-5.

Plessix, R.-E., 2006. A review of the adjoint-state method for computing the gradient of a functional with geophysical applications. Geophys. J. Internat., 167: 495-503.

Pratt, R., 2013. Waveform Tomography, Introduction to Theory and Practice. Western Science, Course notes.

Talagrand, O. and Courtier, P., 1987. Variational assimilation of meteorological observations with the adjoint vorticity equation. I: Theory. Quart. J. Roy. Meteorol. Soc., 113: 1311-1328.

Tarantola, A., 1984. Inversion of seismic reflection data in the acoustic approximation. Geophysics, 49: 1259-1266.

Thomsen, L., 1986. Weak elastic anisotropy. Geophysics, 51: 1954-1966.

Tromp, J., Tape, C. and Liu, Q., 2005. Seismic tomography, adjoint methods, time reversal and banana-doughnut kernels. Geophys. J. Internat., 160: 195-216.

Tsvankin, I., 2012. Seismic Signatures and Analysis of Reflection Data in Anisotropic Media, 3rd Ed. SEG, Tulsa, OK.

Vavryčuk, V., 2005. Focal mechanisms in anisotropic media. Geophys. J. Internat., 161: 334-346.

Vavryčuk, V., 2007. On the retrieval of moment tensors from borehole data. Geophys. Prosp., 55: 381-391.

Virieux, J. and Operto, S., 2009. An overview of full-waveform inversion in exploration geophysics. Geophysics, 74: WCC1-WCC26.